Broadband NIR-emitting Te cluster-doped glass for smart light source towards night-vision and NIR spectroscopy applications

Tan, L.L.; Fu, Y.Q.; Kang, S.L.; Wondraczek, L.; Lin, C.G.; Yue, Yuanzheng

Published in:
Photonics Research

DOI (link to publication from Publisher):
10.1364/PRJ.446416

Publication date:
2022

Document Version
Publisher's PDF, also known as Version of record

Research Article Vol. 10, No. 5 / May 2022 / Photonics Research 1187

PHOTONICS Research

Broadband NIR-emitting Te cluster-doped glass for smart light source towards night-vision and NIR spectroscopy applications

Linling Tan,[1] Yanqing Fu,[1] Shiliang Kang,[1] Lothar Wondraczek,[2,4] Changgui Lin,[1,5] and Yuanzheng Yue[3,6]

[1]Laboratory of IR Materials and Devices, Research Institute of Advanced Technologies, Key Laboratory of Photoelectric Detection Materials and Devices of Zhejiang Province, Ningbo University, Ningbo 315211, China
[2]Otto Schott Institute of Materials Research, University of Jena, 07743 Jena, Germany
[3]Department of Chemistry and Bioscience, Aalborg University, 9220 Aalborg, Denmark
[4]e-mail: lothar.wondraczek@uni-jena.de
[5]e-mail: linchanggui@nbu.edu.cn
[6]e-mail: yy@bio.aau.dk

Received 28 October 2021; revised 28 February 2022; accepted 2 March 2022; posted 3 March 2022 (Doc. ID 446416); published 14 April 2022

Broadband near-infrared (NIR)-emitting materials are crucial components of the next generation of smart NIR light sources based on blue light-emitting diodes (LEDs). Here, we report a Te cluster-doped borate glass, which exhibits ultra-broadband emission around 980 nm with a full-width at half-maximum (FWHM) of 306 nm under blue light excitation. We propose adjustments of glass chemistry and processing condition as a means for topo-chemical tailoring of the NIR photoemission characteristics in such materials. Through implementing strongly reducing conditions during glass melting, Te clusters with broad NIR photoluminescence can be generated and stabilized once the melt is vitrified to the glassy state. Tunability of the NIR emission peak over the wavelength range of 904 to 1026 nm is possible in this way, allowing for fine adjustments of spectral properties relative to the stretching vibrations of common chemical bonds, for example, in water, proteins, and fats. This potentially enables high sensitivity in NIR spectroscopy. We further demonstrate potential application of glass-converted LEDs in night vision.

https://doi.org/10.1364/PRJ.446416

1. INTRODUCTION

Near-infrared (NIR) light with the ability to penetrate deep into organic tissue holds great promise for applications in the medical industry, bio-sensing, food processing, and night-vision technologies [1–3]. Smart NIR light sources could be combined with smart phones to enable convenient devices for NIR sensing and imaging [4,5]. Contrary to traditional NIR light sources such as tungsten halogen lamps and laser diodes, NIR light-emitting diodes (LEds) feature high efficiency and long lifetime, owing to their solid state and compact size, and thus may be used in smart NIR devices. However, the problem is that only a narrow emission bandwidth has been attained in NIR LEDs so far [6,7]. This limits their applications in bio-sensing and food analysis since the spectral characteristics of relevant organic molecules in foodstuffs or, e.g., biological tissues, cover a wide wavelength range [8,9]. Instead, a tunable broadband NIR light source is required. In this regard, NIR phosphors or glasses with tunable broadband emission combined with highly efficient and commercially available blue LED chips were found to be promising components for realizing a compact and low-cost broadband NIR light source [10,11].

The realization of such NIR light sources relies greatly on materials doped with rare-earth (Pr^{3+}, Nd^{3+}, Tm^{3+}, and Er^{3+}) or transition-metal ions (Cr^{3+}, Ni^{2+}, and Mn^{4+}) [12–17]. However, f-f transitions of rare-earth ions, which are relatively independent of crystal field strength and glass composition, lead to narrow absorption and emission bandwidth. Although transition-metal-ion-doped materials exhibit a broader emission band around the NIR region, success on these alternative materials has been limited. For example, Cr^{3+} ion-doped materials, which exhibit broadband emission (~650–1000 nm), have recently been recognized as an ideal NIR luminescent center for obtaining broadband near-infrared emission [11,18,19]. However, it is still difficult to tune the emission peak of Cr^{3+} beyond 900 nm. The NIR spectral region of 900–1100 nm is covered only by the tail of the broadband NIR emission spectrum with very low emission efficiency. Tuning of the emission peaks in this spectral region is critically important for improving the accuracy and breadth of analytical

technology. This is because the primary chemical bonds linked to the vibrational modes in the NIR region are C–H, O–H, and N–H bonds, which are present in protein, water, and fats. Specifically, these bonds exhibit their third stretching overtones at a wavelength of around 920 nm, the second overtone at around 980 nm, and the second overtone at 1086 nm, respectively [8,10]. While these vibrational modes provide access to the constituents of food or biological tissue, it is essential to extend the emission region of the light source toward wavelengths of 1100 nm or above [10].

We note that Te-doped glasses with broadband luminescence have been developed in various types of glasses [20–22]. Unlike the above-mentioned single active ion-doped glasses, the broadband luminescence of Te-doped glasses arises from Te clusters (e.g., Te_2^-, Te_4, and Te_4^{2+}) [23–25]. The archetype photoluminescent (PL) active cluster compound comprises an emissive core and a surrounding ligand arrangement [26,27]. A key role of the ligands is their interaction with the core, which enables tuning the luminescence performance of the Te cluster by controlling its topo-chemical environment [26]. Moreover, Te possesses various types of species (from discrete ions to ions in the cluster) and different valence states (from positive to negative), and they can be easily converted into each other [28–30]. Diverse strategies were proposed to tune the optical performance of the Te NIR centers, such as modifying doping content, modulating chemical composition, and employing high-energy radiation. However, it is still a challenge to extend the emission peak maximum to 900–1100 nm due to the difficulty in stabilizing NIR emitting Te cluster species, as well as in large peak shifts originating from Te_4 or Te_2^- [23,25].

Recently, the topological cage concept has been proposed, by which NIR luminescent Te clusters in the silicate glass matrix can be stabilized, leading to ultra-broadband near-infrared emission in the spectral range of 700–1300 nm with an emission peak maximum at 900 nm [31]. If the size and configuration of the topological cage can be controlled, then new Te clusters will enable tunable NIR emission because those clusters selectively enter the topological cages with specific geometry, size, network modifier type, and network connectivity. Accordingly, topological cages of the germanate glass network can be adjusted by varying the Al_2O_3 content and changing the type of modifying ions so that the cluster configuration can be tailored and thereby a tunable luminescence over a wide range of wavelengths from 600 to 1500 nm can be achieved [32]. However, such Te-doped materials cannot be excited by blue LEDs due to the lack of blue light absorption of the sample. Consequently, developing the Te-activated NIR materials for blue light-pumped LEDs is critical and is also a challenging task.

In this work, we demonstrate that Te-doped borate glass provides the required excitation performance under blue light illumination and exhibits broadband photoemission in the NIR spectral region from 700 to 1500 nm with a peak at 980 nm. We propose a strategy to tune cluster speciation and optimize the spectroscopic properties of Te cluster-doped glass by adjusting glass chemistry, processing conditions, and topological features of the glass matrix. By implementing a reducing atmosphere during glass melting, Te clusters can be stabilized in such materials, giving rise to the broadband photoluminescence. In this way, a tunable emission peak is obtained. Materials produced in this way can be used in glass-converted-LED devices, for example, for night-vision or NIR spectroscopy.

2. EXPERIMENT

A. Sample Preparation

All glasses samples were prepared by melt-quenching from analytical grade reagents B_2O_3, Al_2O_3, K_2CO_3, high purity TeO_2 (99.99%), and carbon (C) (99.95%). We selected two series of borate glasses for Te doping, i.e., $49B_2O_3$-$25Al_2O_3$-$25K_2O$-$1TeO_2$-xC (x represents mole percentage, $x = 0$, 0.05, 0.1, 0.5, 1, 3, and 5), $(79 - y)B_2O_3$-$20Al_2O_3$-yK_2O-$1TeO_2$-3C (y represents mole percentage, $y = 20$, 25, 30, 35, and 40). In the following, these are denoted as B–xC and B–yK, respectively. Appropriate powder batches were prepared from the above-mentioned raw materials and weighted to yield ~30 g of glass, ground and filled into alumina crucibles. Melting was then conducted at 1400°C for 0.5 h in air. Glass samples were finally obtained by pouring the melts onto a cold plate of stainless steel and pressing with another steel plate in order to increase the cooling rate. The obtained glass slabs were cut into pieces of about 1 cm × 1 cm × 0.2 cm and polished to optical grade.

B. Material Characterization

Optical transmittance spectra were recorded on a Perkin Elmer Lambda-900 UV-Vis-NIR spectrophotometer over the spectral range of 200 to 3200 nm. Photoluminescence spectroscopy measurements (static excitation and emission spectra) were conducted on an Edinburgh FLS920 spectrofluorometer equipped with a static 450 W Xe lamp as excitation sources. Transmission electron microscopy (TEM) and high-resolution transmission microscopy (HRTEM) images were collected with a JEOL JEM-2100F microscope. Vibrational spectroscopic measurements were performed on a Renishaw InVia Raman spectrometer excited with a 532 nm laser at an output power of ~5 mW. The magic angle spinning nuclear magnetic resonance (MAS NMR) spectra were collected on a Bruker spectrometer (AVANCE III HD 400) at a magnetic field strength of 9.4 T with a 4 mm MAS probe. ^{11}B MAS NMR spectra were recorded at a frequency of 128.38 MHz with a 4.5 μs pulse using 15 s recycle delays to prevent saturation. Finally, electron paramagnetic resonance (EPR) spectra were collected with an X-band spectrometer (ELEXSYS, Bruker A300) using a microwave power of 1 mW and modulation amplitude of 3 G. The electroluminescence spectra and performances of glass-converted NIR-LEDs were examined using a photoelectric measuring system (HAAS 2000, 350–1100 nm, EVERFINE). The drive-current for the NIR LED was within 100–800 mA. Photographs for the application of the NIR LED device were taken with an NIR camera (DinoCapture 2.0).

3. RESULTS AND DISCUSSION

Borate glasses possess a broad variety of superstructural units such as boroxol, borate or diborate rings, metaborate rings or

chains, and pyro- or orthoborate groups [33,34]. The fractions of these units can be adjusted by not only varying the type and fraction of network modifiers but also changing the melting condition and thermal history [34,35]. This provides an opportunity to control the topological environment of Te cluster species for tunable luminescence when these species are incorporated into the borate matrix. However, Te-related photoluminescence such as in silicate or phosphate matrices was not yet reported in this group of materials [36]. In the present work, the carbon-induced melt-reduction results in broad photoluminescence at 904 nm in the quenched glass [full-width at half-maximum (FWHM) of ~240 nm, 435 nm excitation, see Fig. 1(a)]. The extent of melt reduction, which depends on the amount of added carbon, determines the variation in this emission band, in particular, in band intensity. There appears to be an optimum amount of C of about 3% (mole fraction), i.e., the optimum reduction extent, which generates the Te cluster species with the most efficient broadband NIR emission. The same phenomenon was also observed when using the secondary excitation bands at 645 nm [see Figs. 1(b) and 1(c)]. The quantitative effects of the added C strongly depend on the individual melting conditions, e.g., the ambient atmosphere, humidity, ventilation, and raw material chemistry. If the reduction condition is too strong, then metallic Te could form, which is not PL active.

TEM analysis on the glass B-3C indicates the presence of both the spherical Te particles with a diameter of ~1 to 3 nm [light spots in Fig. 1(d)] and the larger, metallic particles [Fig. 1(e)]. A transmission electron microscopy-energy dispersive spectrometer (TEM-EDS) scan across the light spots [Fig. 1(f)] implies higher Te concentration and oxygen depletion in this region, confirming that these spots are indeed Te particles.

While the initial NIR photoluminescence spectra reveal only one single emission center, the transmission spectra of glasses with different amounts of added C point to the presence of multiple absorbing species [Fig. 1(g)]. The glass without C exhibits no notable absorption in the considered spectral range but does exhibit the occurrence of four absorption bands because of melt reduction. Notably, no peak can be observed in the C-containing glass without Te doping, indicating that these absorption bands are attributed to Te centers. It is seen in the inset of Fig. 1(g) that the appearance of the glass gradually changes from colorless to brownish with the increasing C content. The absorption bands at 350 and 980 nm originate from exciton transition and Te_4, respectively [36,37]. The bands at 440 and 640 nm were previously attributed to Te_2 and Te_2^-, respectively, and these chemical states were also considered to be the source of Te-related NIR emission [23,38]. However, for the present materials, we did not find paramagnetic Te_2^- by room-temperature electron paramagnetic resonance (EPR) spectroscopy [Fig. 1(h)]. Based on previous density functional theory (DFT) calculations, the Te_2 clusters exhibit ultraviolet and visible emission outside the NIR spectral region [32]. The emission at 904 nm indicates the presence of D_{2h}–Te_4 with space group Pmmm as the responsible emission centers [31,32]. The absorption bands at 440 and 640 nm correspond to the higher-lying excitation bands of the 904 nm emission, suggesting that these bands also originate from the D_{2h}–Te_4. In strong contrast, no luminescence under 980 nm laser diode (LD) excitation can be observed, indicating that the chemical state of Te_4 is non-luminous (NL–Te_4).

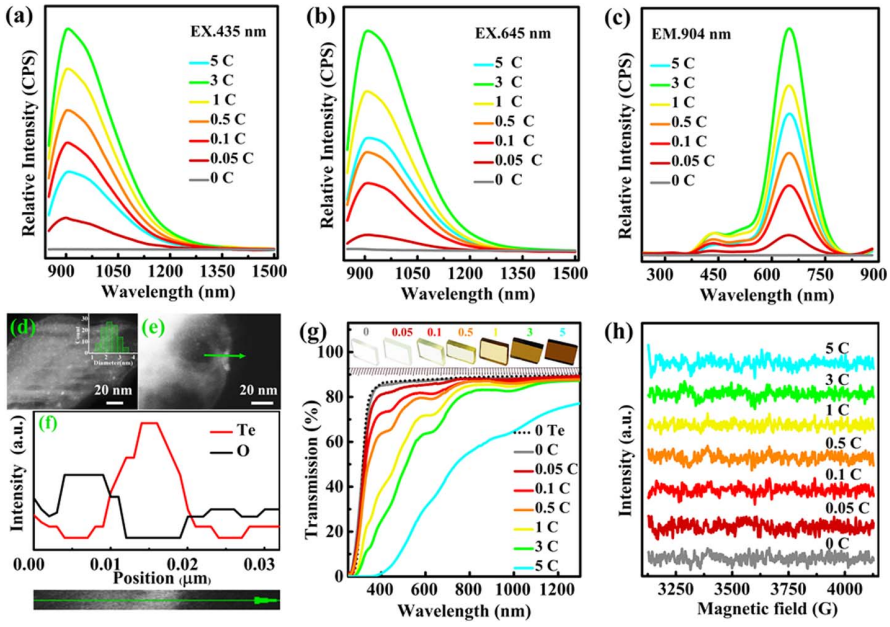

Fig. 1. Occurrence and identification of Te clusters. Emission spectra upon (a) 435 nm and (b) 645 nm excitation. (c) The excitation spectra monitored at 904 nm of glass samples B–xC (x = 0, 0.05, 0.1, 0.5, 1, 3, and 5). (d) and (e) The TEM micrograph of sample B-3C. (f) The EDS line scan along the path indicated in (e) for Te and O elements. (g) The optical transmission of glass samples B–xC (x = 0, 0.05, 0.1, 0.5, 1, 3, and 5) compared with sample B-3C without Te doping. (h) The EPR spectra of glass samples B–xC (x = 0, 0.05, 0.1, 0.5, 1, 3, and 5).

By introducing network modifiers that possess less localized bonds with predominantly ionic bonds, compared to network formers, we can control the degree of network connectivity in oxide glasses. Alkali ions, particularly K_2O, are typical network-modifying species in borate glasses [4,39,40]. By varying the content of the network modifiers, we can tailor the Te-related spectroscopic properties in such borate matrices. When the K_2O content increases from 25% to 30% (mole fraction), the excitation bands at 435, 500, and 645 nm emerge with shifting positions toward shorter wavelengths [Fig. 2(a)]. The excitation bands at 435 and 645 nm correspond to the absorption at 440 and 640 nm, respectively, originating from D_{2h}–Te_4. With a further increase of K_2O, the excitation band at 645 nm decreases in intensity, while the blue excitation band at 435 nm increases, broadens, and red shifts to 500 nm. Furthermore, a new band is observed at about 330 nm for $K_2O > 30\%$. This variation in the excitation bands reflects changes in the characteristics (e.g., size and valence state) of the Te species.

The characteristics of the NIR emission can be tuned by tuning the Te speciation, as shown in Figs. 2(b) and 2(c). Upon 500 nm excitation, the emission intensity increases with K_2O content, and the FWHM is extended from 253 to 306 nm. In addition, we can observe a pronounced red shift from 904 nm for sample B-25K to 1026 nm for B-40K [Fig. 2(b)]. Upon excitation at 435 or 645 nm, the intensity of the photoemission increases with the K_2O content, reaching a maximum in B-30K, and then decreases with the further increasing K_2O [Fig. 2(c)]. The emission peaks monotonically shift to longer wavelengths and become broader, in particular, from sample B-35K to B-40K. Upon excitation at 330 nm, the K_2O content dependence of the luminescence intensity is consistent with that of the excitation intensity.

The Raman spectra of the K_2O series are shown in Fig. 2(d). Their features are in good agreement with those reported in previous studies of the well-known alkali alumino borate glasses [33,39]. In general, K_2O addition leads to a band shift to lower energy, reflecting the decreasing network connectivity. Furthermore, some changes occur in borate coordination and between metaborate chains and rings, favoring lower cross-linking with increasing K_2O content [34,41]. Considering the Te speciation, a weak band emerges at 214 cm^{-1}, arising from the Te_2 in sample B-25K. Its intensity increases in B-30K with increasing K_2O content but subsequently decreases in B-40K. In parallel, the band at 178 cm^{-1} resulting from D_{3h}–Te_6 appears in B-30K and then decreases [28,42]. This indicates that smaller Te-clusters (Te_2 and, potentially, Te_4) grow into Te_6 and transform into later semi-metallic Te or are dissolved as

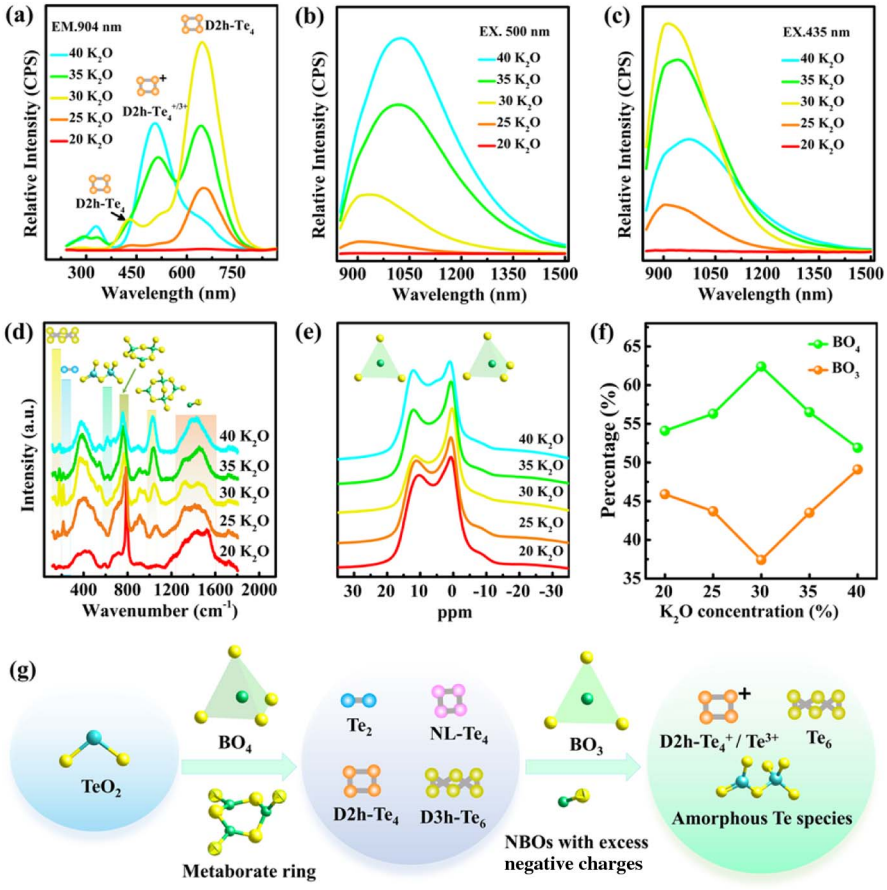

Fig. 2. Tunable luminescence behavior of Te clusters and manipulation of Te speciation through network modifiers. (a) The excitation spectra monitored at 904 nm. The emission spectra upon (b) 500 and (c) 435 nm excitation. (d) The Raman spectra and (e) the ^{11}B MAS NMR spectra of samples B–yK (y = 20, 25, 30, 35, and 40). (f) The occurrence of BO_3 and BO_4 approximated from NMR band integration. (g) The schematic for the evolution of Te clusters with the increasing K_2O content.

TeO_2 in the glass matrix. This process leads to a new band at 620 cm^{-1}, which corresponds to the axial symmetric stretching mode of the (Te_{ax}–O) in the TeO_4 tetrahedra [22,43]. Based on previous DFT calculations, the Te_6 clusters exhibit visible emission (at 457 nm), indicating that the Te_6 clusters do not contribute to the NIR emission [32].

Boron speciation is quantified using ^{11}B NMR to determine the fractions of the BO_4 tetrahedra and the BO_3 trigonal groups [Figs. 2(e) and 2(f)] [44]. Tetrahedral BO_4 is the dominant species in all samples. However, a local maximum (minimum in BO_3) occurs for the intermediate K_2O content in sample B-30K, corroborating the Raman observations and previous studies of similar alumino borate glasses.

Based on the structure characterizations of the studied glasses, a mechanism for the evolution of the Te clusters is described in Fig. 2(g). This mechanism involves three aspects: 1) network topology related to rings and chains, 2) negatively charged environment due to the presence of non-bridged oxygen species (NBOs), and 3) local cation acidity due to variations in the presence of potassium. Increasing the fraction of network modifiers causes an increase in the number of NBOs, and thereby creates the negatively charged local environment. Thus, more positive charges are required for charge balance, leading to an increase in the valence state of Te. Then, the Te may be incorporated into the glass network in the form of TeO_2, forming a classical boro-tellurite matrix. As a result, the Te-related NIR photoemission excited at 435 and 645 nm (D_{2h}–Te_4) disappears. On the other hand, as long as TeO_2 does not form (i.e., oxidation to Te^{4+} does not occur), the oxidizing effect favors the formation of Te clusters with higher valence, thereby enhances the blue light excitation band and causes an increase in the intensity of the Te NIR emission excited at 500 nm. We attribute these latter excitation bands to species such as D_{2h}–Te_4^+ or Te_4^{3+}, which have previously been demonstrated for excitation at 508 nm based on the time-dependent density functional theory (TDDFT) calculation [24]. The observed increase of NIR activity from Te clusters is attributed to the fact that the metaborate chains are converted into rings, and hence create favorable spatial conditions for limiting Te aggregation to prevent the formation of semi-metallic Te particles. Considering the boron anomaly, borate groups transform from BO_3 into BO_4, leading to higher network connectivity and, assumedly, stabilizing Te clusters. In this way, the occurrence of Te_4 species is tailored, leading to a tunable NIR emission and the enhancement of NIR emission under blue light excitation.

An NIR LED with a broadband NIR light source was fabricated by covering a commercial 460 nm LED chip with the Te-doped borate glass B-40K. When the NIR LED is lit, images of the NIR LED were obtained using an NIR camera with and without an 800 nm filter, respectively [inset of Fig. 3(a)]. The electroluminescence spectrum of the NIR LED under different driving currents shows a super broadband NIR emission peaking at 980 nm [Fig. 3(a)]. The NIR emission output power increases with increasing current and reaches 22.25 mW in the NIR region at 700–1100 nm under a current of 800 mA [Fig. 3(b)]. The conversion efficiency decreases from 21.2% to 15.9% as the current increases from 100 to 800 mA. To be competitive with other types of NIR light sources, the performance of the NIR LED should be further optimized. A blue LED chip with higher photoelectric efficiency can be used to improve the output power of the NIR LED since the photoelectric efficiency of the employed blue LED chip is not very high (e.g., only 11.4% at 800 mA). On the other hand, only 70.5% of the NIR emission was obtained because of the limitation of the measurement range (up to 1100 nm) [Fig. 3(c)]. If the 29.5% unmeasured part is considered, the actual NIR output power should be 31.56 mW at 800 mA.

An NIR LED device was assembled by covering a long wave-pass filter (800 nm) on the NIR LED, as illustrated in Fig. 4(a). Figure 4(b) shows photographs of a flower, of a tomato, and of a succulent plant, which were taken under natural light and the NIR LED device light, implying a potential application of the Te cluster-doped borate glass in night-vision technology. Compared with other kinds of NIR light sources, the NIR emission peak at 980 nm has a higher relative intensity, and its position is much closer to those of the absorption peaks of common chemical bonds. This holds the promise of less noise and interference for higher detection sensitivity. For demonstration, we used raw slices of pork tissue [Fig. 4(c)]. For this, the NIR LED device was covered by a slice of the tissue. The thickness of the slice was varied between tests so that the net NIR emission intensity was recorded as a function of cover thickness. Figure 4(d) shows that the luminescence is partly absorbed in the raw pork tissue. The emission intensity decreases to 40% when the pork thickness increases from 0 to

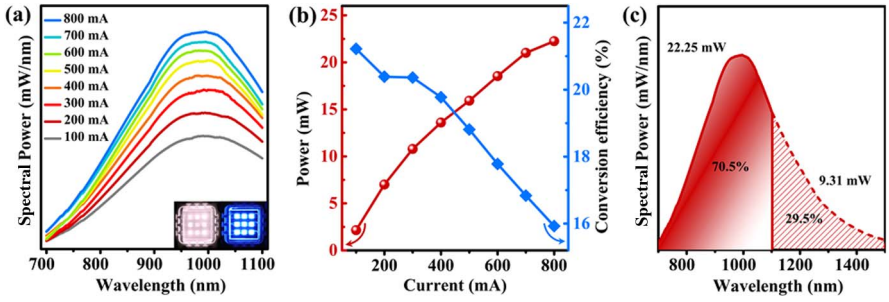

Fig. 3. Electroluminescence performance of Te cluster-doped glass converted-LED device. (a) The electroluminescence spectra of the as-fabricated NIR LED based on B-40K under different driven currents. Inset: photograph of the fabricated NIR LED under natural light and the NIR light (with an 800 nm filter). (b) The driven current dependence of output powers and conversion efficiencies. (c) The electroluminescence spectrum fitted by the Gaussian formula.

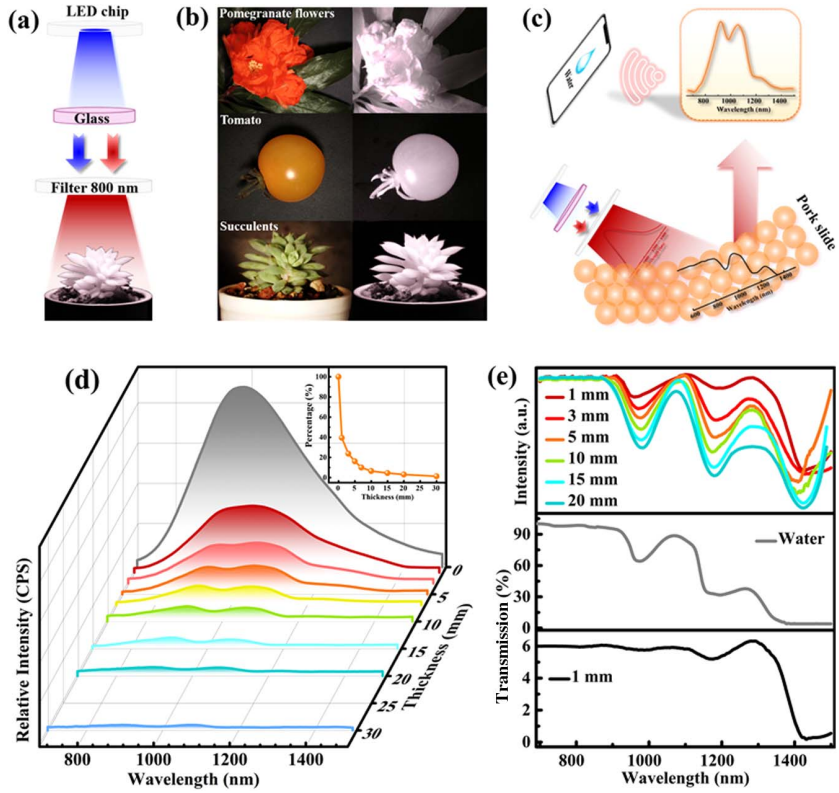

Fig. 4. NIR applications of Te cluster-doped glass converted-LED device. (a) The working schematic of the NIR LED device. (b) Photographs of a flower, of a tomato, and of a succulent plant under natural light (left panels) and the NIR LED device (right panels). (c) The schematic diagram of the NIR LED biological penetration experiment. (d) The emission spectra of the NIR light after passing through different thicknesses of pork slices. Inset: the intensity ratio between the NIR LED emission after and before passing through pork slices as a function of the thicknesses of the pork slices. (e) The upper panel, calculated transmission spectra of the NIR LED light after passing through the different thicknesses of pork slices. The middle and lower panels, measured transmission spectra of the water and 1 mm pork slice, respectively.

1 mm and decreases further to 2% for the 30 mm slice [Inset of Fig. 4(d)], indicating the degree of tissue penetration. Transmission spectra of the NIR LED light after passing through the different layers of tissue slices are shown in the upper panel of Fig. 4(e). The shape of the calculated transmission spectra is different from that of the water measured by the UV-Vis-NIR spectrometer [middle panel in Fig. 4(e)], especially for the intensity ratio of the absorption band at 980 nm band to that at 1180 nm for the 1 mm pork slice with lower water content. Assumedly, even a weak absorption at 980 nm measured by the UV-Vis-NIR spectrometer could be detected [lower panel of Fig. 4(e)], since the Te cluster-doped glass exhibits strong emission intensity around 980 nm, which contributes to the high detection sensitivity.

4. CONCLUSIONS

A series of luminescent, tunable NIR-emitting Te cluster-doped borate glasses with a super-broad excitation band from 250 to 850 nm were designed and synthesized. Upon blue light excitation, the Te cluster-doped glass was used to generate an ultra-broadband emission centered at 980 nm with a large FWHM of 306 nm. By manipulating glass chemistry, processing, and topological features of the glass matrix, we were able to tailor active Te cluster centers, and thereby achieved the tunable NIR emission peak with a center position varying from 904 to 1026 nm. The spectral region of this peak matches the location of the stretching vibrations of the common chemical bonds in water, protein, and fats.

Funding. National Natural Science Foundation of China (62105170, 62122039); K. C. Wong Magna Fund in Ningbo University.

Disclosures. The authors declare no conflicts of interest.

Data Availability. Data underlying the results presented in this paper are not publicly available at this time but may be obtained from the corresponding authors upon reasonable request.

REFERENCES

1. A. T. Eggebrecht, S. L. Ferradal, A. Robichaux-Viehoever, M. S. Hassanpour, H. Dehghani, A. Z. Snyder, T. Hershey, and J. P. Culver, "Mapping distributed brain function and networks with diffuse optical tomography," Nat. Photonics **8**, 448–454 (2014).
2. B. Zeng, Z. Huang, A. Singh, Y. Yao, A. K. Azad, A. D. Mohite, A. J. Taylor, D. R. Smith, and H.-T. Chen, "Hybrid graphene metasurfaces for high-speed mid-infrared light modulation and single-pixel imaging," Light Sci. Appl. **7**, 51 (2018).

3. K. T. Ly, R.-W. Chen-Cheng, H.-W. Lin, Y.-J. Shiau, S.-H. Liu, P.-T. Chou, C.-S. Tsao, Y.-C. Huang, and Y. Chi, "Near-infrared organic light-emitting diodes with very high external quantum efficiency and radiance," Nat. Photonics **11**, 63–68 (2017).
4. A. Zampetti, A. Minotto, and F. Cacialli, "Near-infrared (NIR) organic light-emitting diodes (OLEDs): challenges and opportunities," Adv. Funct. Mater. **29**, 1807623 (2019).
5. C. Dincer, R. Bruch, E. Costa-Rama, M. T. Fernández-Abedul, A. Merkoçi, A. Manz, G. A. Urban, and F. Güder, "Disposable sensors in diagnostics, food, and environmental monitoring," Adv. Mater. **31**, 1806739 (2019).
6. R. Filippo, E. Taralli, and M. Rajteri, "LEDs: sources and intrinsically bandwidth-limited detectors," Sensors **17**, 1673 (2017).
7. X. Zhao and Z.-K. Tan, "Large-area near-infrared perovskite light-emitting diodes," Nat. Photonics **14**, 215–218 (2020).
8. Y. Dixit, M. P. Casado-Gavalda, R. Cama-Moncunill, X. Cama-Moncunill, M. Markiewicz-Keszycka, P. J. Cullen, and C. Sullivan, "Developments and challenges in online NIR spectroscopy for meat processing," Compr. Rev. Food Sci. Food Saf. **16**, 1172–1187 (2017).
9. F. F. Jöbsis, "Noninvasive, infrared monitoring of cerebral and myocardial oxygen sufficiency and circulatory parameters," Science **198**, 1264–1267 (1977).
10. G. N. A. De Guzman, S. F. Hu, and R. S. Liu, "Enticing applications of near-infrared phosphors: review and future perspectives," J. Chin. Chem. Soc. **68**, 206–215 (2021).
11. L. Zhang, D. Wang, Z. Hao, X. Zhang, G.-H. Pan, H. Wu, and J. Zhang, "Cr^{3+}-doped broadband NIR garnet phosphor with enhanced luminescence and its application in NIR spectroscopy," Adv. Opt. Mater. **7**, 1900185 (2019).
12. J. Chen, C. Guo, Z. Yang, T. Li, and J. Zhao, "$Li_2SrSiO_4:Ce^{3+}$, Pr^{3+} phosphor with blue, red, and near-infrared emissions used for plant growth LED," J. Am. Ceram. Soc. **99**, 218–225 (2016).
13. A. Benayas, B. del Rosal, A. Pérez-Delgado, K. Santacruz-Gómez, D. Jaque, G. A. Hirata, and F. Vetrone, "Nd:YAG near-infrared luminescent nanothermometers," Adv. Opt. Mater. **3**, 687–694 (2015).
14. M. Nyk, R. Kumar, T. Y. Ohulchanskyy, E. J. Bergey, and P. N. Prasad, "High contrast *in vitro* and *in vivo* photoluminescence bioimaging using near infrared to near infrared up-conversion in Tm^{3+} and Yb^{3+} doped fluoride nanophosphors," Nano Lett. **8**, 3834–3838 (2008).
15. E. T. Basore, H. Wu, W. Xiao, G. Zheng, X. Liu, and J. Qiu, "High-power broadband NIR LEDs enabled by highly efficient blue-to-NIR conversion," Adv. Opt. Mater. **9**, 2001660 (2021).
16. Z. Liao, H. Xu, W. Zhao, H. Yang, J. Zhong, H. Zhang, Z. Nie, and Z.-K. Zhou, "Energy transfer from Mn^{4+} to Mn^{5+} and near infrared emission with wide excitation band in $Ca_{14}Zn_6Ga_{10}O_{35}$:Mn phosphors," Chem. Eng. J. **395**, 125060 (2020).
17. F. Liu, Y. Liang, Y. Chen, and Z. Pan, "Divalent nickel-activated gallate-based persistent phosphors in the short-wave infrared," Adv. Opt. Mater. **4**, 562–566 (2016).
18. M.-H. Fang, P.-Y. Huang, Z. Bao, N. Majewska, T. Leśniewski, S. Mahlik, M. Grinberg, G. Leniec, S. M. Kaczmarek, C.-W. Yang, K.-M. Lu, H.-S. Sheu, and R.-S. Liu, "Penetrating biological tissue using light-emitting diodes with a highly efficient near-infrared $ScBO_3:Cr^{3+}$ phosphor," Chem. Mater. **32**, 2166–2171 (2020).
19. Z. Jia, C. Yuan, Y. Liu, X.-J. Wang, P. Sun, L. Wang, H. Jiang, and J. Jiang, "Strategies to approach high performance in Cr^{3+}-doped phosphors for high-power NIR-LED light sources," Light Sci. Appl. **9**, 86 (2020).
20. P. Penprapa, "*Nir Luminescence Characteristics of Te-Doped Glasses*," Thesis (Suranaree University of Technology, 2009).
21. E. M. Dianov, S. V. Alyshev, A. V. Shubin, V. F. Khopin, and A. N. Gur'yanov, "IR luminescence of tellurium-doped silica-based optical fibre," Quantum Electron. **42**, 189–191 (2012).
22. L. Tan, S. Kang, Z. Pan, Y. Zhang, Y. Yue, S. Xu, M. Peng, and L. Wondraczek, "Topo-chemical tailoring of tellurium quantum dot precipitation from supercooled polyphosphates for broadband optical amplification," Adv. Opt. Mater. **4**, 1624–1634 (2016).
23. S. Khonthon, S. Morimoto, Y. Arai, and Y. Ohishi, "Luminescence characteristics of Te- and Bi-doped glasses and glass-ceramics," J. Ceram. Soc. Jpn. **115**, 259–263 (2007).
24. H.-T. Sun, Y. Sakka, N. Shirahata, M. Fujii, and T. Yonezawa, "Near-infrared photoluminescence from molecular crystals containing tellurium," J. Mater. Chem. **22**, 24792–24797 (2012).
25. L. Tan, J. C. Mauro, S. Xu, Z. Yang, and M. Peng, "Unusual thermal response of tellurium near-infrared luminescence in phosphate laser glass," Opt. Lett. **43**, 4823–4826 (2018).
26. H. Wu, X. He, B. Yang, C.-C. Li, and L. Zhao, "Assembly-induced strong circularly polarized luminescence of spirocyclic chiral silver(I) clusters," Angew. Chem. Int. Ed. **60**, 1535–1539 (2021).
27. W.-M. He, Z. Zhou, Z. Han, S. Li, Z. Zhou, L.-F. Ma, and S.-Q. Zang, "Ultrafast size expansion and turn-on luminescence of atomically precise silver clusters by hydrogen sulfide," Angew. Chem. Int. Ed. **60**, 8505–8509 (2021).
28. B. C. Pan, "Geometric structures, electronic properties, and vibrational frequencies of small tellurium clusters," Phys. Rev. B **65**, 085407 (2002).
29. G.-G. Lindner, K. Witke, H. Schlaich, and D. Reinen, "Blue-green ultramarine-type zeolites with dimeric tellurium colour centres," Inorg. Chim. Acta **252**, 39–45 (1996).
30. J. Beck, "Rings, cages and chains—the rich structural chemistry of the polycations of the chalcogens," Coord. Chem. Rev. **163**, 55–70 (1997).
31. L. Tan, L. Huang, and M. Peng, "D2h-symmetric tetratellurium clusters in silicate glass as a broadband NIR light source for spectroscopy applications," ACS Appl. Mater. Interface **12**, 51628–51636 (2020).
32. L. Tan, L. Huang, C. He, J. C. Mauro, M. Peng, X.-B. Yang, and Y. Yue, "Tailoring cluster configurations enables tunable broad-band luminescence in glass," Chem. Mater. **32**, 8653–8661 (2020).
33. W. L. Konijnendijk, "The structure of borosilicate glasses," Thesis (Eindhoven University of Technology, 1975).
34. D. Möncke, E. I. Kamitsos, D. Palles, R. Limbach, A. Winterstein-Beckmann, T. Honma, Z. Yao, T. Rouxel, and L. Wondraczek, "Transition and post-transition metal ions in borate glasses: borate ligand speciation, cluster formation, and their effect on glass transition and mechanical properties," J. Chem. Phys. **145**, 124501 (2016).
35. Z. Y. Yao, D. Möncke, E. I. Kamitsos, P. Houizot, F. Célarié, T. Rouxel, and L. Wondraczek, "Structure and mechanical properties of copper-lead and copper-zinc borate glasses," J. Non-Cryst. Solids **435**, 55–68 (2016).
36. S. Khonthon, P. Punpai, S. Morimoto, Y. Arai, T. Suzuki, and Y. Ohishi, "On the near-infrared luminescence from TeO_2 containing borate glasses," J. Ceram. Soc. Jpn. **116**, 829–831 (2008).
37. P. Hassanzadeh, C. Thompson, and L. Andrews, "Absorption spectra of tellurium clusters in solid argon," J. Chem. Phys. **96**, 8246–8249 (1992).
38. S. V. Alyshev, K. E. Ryumkin, A. V. Shubin, O. I. Medvedkov, E. M. Dianov, , V. F. Khopin, and A. N. Gur'yanov, "Fibre laser based on tellurium-doped active fibre," Quantum Electron. **44**, 95–97 (2014).
39. G. D. Chryssikos, E. I. Kamitsos, A. P. Patsis, and M. A. Karakassides, "On the structure of alkali borate glasses approaching the orthoborate composition," Mater. Sci. Eng. B **7**, 1–4 (1990).
40. C. Calahoo and L. Wondraczek, "Ionic glasses: structure, properties and classification," J. Non-Cryst. Solids X **8**, 100054 (2020).
41. B. N. Meera, A. K. Sood, N. Chandrabhas, and J. Ramakrishna, "Raman study of lead borate glasses," J. Non-Cryst. Solids **126**, 224–230 (1990).
42. V. V. Poborchii, "Polarized Raman and optical absorption spectra of the mordenite single crystals containing sulfur, selenium, or tellurium in the one-dimensional nanochannels," Chem. Phys. Lett. **251**, 230–234 (1996).
43. L. Koudelka, I. Rösslerová, Z. Černošek, P. Mošner, L. Montagne, and B. Revel, "The structural role of tellurium dioxide in lead borophosphate glasses," J. Non-Cryst. Solids **401**, 124–128 (2014).
44. L. Wondraczek, S. Sen, H. Behrens, and R. E. Youngman, "Structure-energy map of alkali borosilicate glasses: effects of pressure and temperature," Phys. Rev. B **76**, 014202 (2007).